Vertical coherence in mantle heterogeneity from global seismic data

L. Boschi[1,2] and T. W. Becker[3]

Received 11 August 2011; revised 15 September 2011; accepted 22 September 2011; published 25 October 2011.

[1] The vertical coherence of mantle structure is of importance for a range of dynamic issues including convective mass transport and the geochemical evolution of Earth. Here, we use seismic data to infer the most likely depth ranges of strong, global changes in the horizontal pattern of mantle heterogeneity. We apply our algorithm to a comprehensive set of measurements, including various shear- and compressional-wave delay times and Love- and Rayleigh-wave fundamental mode and overtone dispersion, so that tomography resolution is as high as possible at all mantle depths. We find that vertical coherence is minimum at ~100 km and ~800 km depths, corresponding to the base of the lithosphere and the transition between upper and lower mantle, respectively. The D″ layer is visible, but not as prominent as the shallower features. The rest of the lower mantle is, essentially, vertically coherent. These findings are consistent with slab stagnation at depths around, and perhaps below, the 660-km phase transition, and inconsistent with global, chemically distinct, mid-mantle layering. **Citation:** Boschi, L., and T. W. Becker (2011), Vertical coherence in mantle heterogeneity from global seismic data, *Geophys. Res. Lett.*, *38*, L20306, doi:10.1029/2011GL049281.

1. Introduction

[2] With the availability of enormous databases of digital seismic observations, seismic tomography has evolved to the point of providing a data- and methodology-invariant picture of the global, very long wavelength pattern of mantle structure [e.g., *Becker and Boschi*, 2002]. Tomography models are less consistent at shorter spatial scale lengths, and discrepancies are important enough to result in different theories of the Earth [e.g., *Tackley*, 2000]. For example, many authors now agree that slabs penetrate into the lower mantle under some present or past converging plate boundaries [e.g., *Grand et al.*, 1997]. Yet, it is often suggested that this is not a global phenomenon, and that, at least at some locations, subducting plates stagnate and possibly break at the base of the upper mantle [e.g., *van der Hilst and Seno*, 1993; *Fukao et al.*, 2001; *Obayashi et al.*, 2009].

[3] Stagnation of slabs is typically discussed in the context of the 660-km phase change, but may also be found at larger depths, perhaps closer to ~1000 km [e.g., *Obayashi et al.*, 2009], or in the ~1200–2000-km depth range, where mineral physics suggests that the high-spin to low-spin transition of iron might indirectly hinder mantle flow [e.g., *Bower et al.*, 2009]. *Kellogg et al.* [1999] placed the top of a hypothetical, intrinsically dense global layer ("hot abyssal layer") in a similar depth range (~1600 km). A related subject is that of the origin of hot spots, which are often associated with "primary" or "secondary" plumes that interact with any deep mantle chemical heterogeneity [e.g., *Tackley*, 2000; *Courtillot et al.*, 2003; *Boschi et al.*, 2007].

[4] Owing to the limited spatial resolution of tomography, attempts to address these issues through the analysis of individual mapped features have been inconclusive. Several studies have then addressed the underlying general question of vertical mass transport in the mantle in a global, statistical way: for example *Gu et al.* [2003] used vertically continuous versus discontinuous tomographic parameterizations to study the change in power spectral character across the 660 km discontinuity; *Dziewonski et al.* [2010] later gave a more thorough discussion of the vertical dependence of the mantle power spectrum.

[5] The vertical coherence of tomography has also been quantified by the radial correlation between its structure at different depths [e.g., *Puster and Jordan*, 1997; *Tackley*, 2002], or calculating the correlation between tomography and dynamic models of slab or plume distribution [*Boschi et al.*, 2007]. *Becker and Boschi* [2002] analyzed a number of existing global tomography models, finding minima in vertical coherence at upper mantle discontinuities (with the most prominent one always at 660 km) and an essentially vertically coherent lower mantle. We have repeated the analysis of *Becker and Boschi* [2002] on more recent models, confirming their results.

[6] Here, we do not test any published tomography model. Rather, we use global databases of body and surface waves to more directly estimate the depth ranges of likely global changes in the horizontal pattern of mantle heterogeneity, more effectively and less constrained by a priori assumptions than typical tomography. The main component of our method is an updated version of voxel-tomography software [*Boschi and Dziewonski*, 1999], with much finer vertical resolution and capable of handling surface-wave as well as body-wave data. We apply it to a number of different seismic databases, and discuss the implications of our results in terms of vertical flow throughout the Earth's mantle.

2. Data

[7] Differences between tomography models must arise, to some extent, from differences in the approaches used to extract relevant data from seismograms. To identify robust

[1]Institute of Geophysics, ETH Zurich, Zurich, Switzerland.
[2]Institute of Theoretical Physics, University of Zurich, Zurich, Switzerland.
[3]Department of Earth Sciences, University of Southern California, Los Angeles, California, USA.

0094-8276/11/2011GL049281

features, we applied our algorithm to data observed in different ways by different authors. To maximize resolution at all depths, we include both body-wave travel time and surface-wave dispersion measurements.

[8] We considered *P*-wave travel times from *Antolik et al.* [2001], *S*-wave travel times from *Houser et al.* [2008] and *Ritsema et al.* [2011], and the dispersion of surface-wave fundamental modes and overtones from *Visser et al.* [2008] and *Ritsema et al.* [2011]. All observations were expressed as perturbations to PREM. For both body- and surface-wave data, we compute and employ summary rays associated with equal-area (2° × 2° at the equator) source and receiver bins.

3. Tomography Toolbox

[9] Following *Boschi and Dziewonski* [1999], we parameterize the mantle horizontally in terms of approximately equal-area pixels of 5° × 5° lateral extent at the equator. Our software allows for a finer horizontal grid, but 5° × 5° is enough given the presumed global resolution of mantle structure. Vertically, mantle structure is described by 50 vertical layers: this means that the vertical size of the resulting voxels is ~ ten times smaller than the horizontal one. Vertical overparameterization, and the consequent anisotropy in nominal resolution, is necessary to our algorithm (section 5).

[10] The combination of Love- and Rayleigh-wave data is strongly sensitive to lateral variations in radial anisotropy, known to be significant in the upper mantle [e.g., *Nataf et al.*, 1984]. The sensitivity of surface waves to horizontally (v_{SH}) and vertically polarized shear velocity (v_{SV}) is computed as described by *Boschi and Ekström* [2002]; we employ Crust5.1 [*Mooney et al.*, 1998] as the reference crustal model for its consistency with our 5° × 5° parameterization. When inverting body-wave data jointly with surface-wave ones, we follow *Woodhouse* [1981] to describe the different sensitivity of *S* waves to v_{SH} and v_{SV}. Yet, because most of the *S*-wave data available to us are observed on the horizontal component of seismic records, our sensitivity to the lower mantle is limited to v_{SH}. Rather than postulating isotropy, or attempting to constrain the elusive pattern of deep mantle anisotropy [e.g., *Panning et al.*, 2010], we neglect the (relatively few) v_{SV}-sensitive body-wave data (*SKS*, etc.) and accordingly limit our discussion throughout the rest of this study to models of v_{SH} anomalies. When inverting sets of body-wave travel times alone, we neglect anisotropy and map isotropic v_S perturbations only.

[11] The linear inverse problem associated with the chosen parameterization is mixed-determined (~10^6 summary observations in the joint *S*- and surface-wave case) and characterized by 198,800 free parameters (half as many in the isotropic case). We regularize it via roughness damping and least squares-invert it as described by *Boschi and Dziewonski* [1999]. The regularization parameter is chosen so that the long-wavelength features shared by all recent tomography models are confirmed by our inversions. We have verified that the results presented in the following are not much perturbed by changes in the regularization scheme (e.g., a fivefold increase in the strength of vertical roughness damping, while horizontal roughness damping is left unchanged).

4. Classic Tomography Inversions

[12] Figures 1 and 2 summarize how global tomography "sees" the Earth's mantle. The checkerboard test in Figure 1a was conducted with synthetic *S*-wave data, including direct (*S*) and multiply reflected (*SS*, *SSS*, *SSSS*, *sS*, *sSS* and *sSSS* as by *Ritsema et al.* [2011]) delay times. The input model is a degree $l = 10$, order $m = 5$ real spherical harmonic with minimum and maximum values of ±3%, and changes in sign at ~600, ~1200, ~1900 and ~2500 km depth. We next combined this synthetic database with one based on the fundamental- and higher-mode surface-wave database of *Visser et al.* [2008], and the same input model: the results (v_{SH} component only) are shown in Figure 1b. Before inversion, normally distributed random noise (with realistic standard deviations of 3 s for *S* waves [e.g., *Della Mora et al.*, 2011] and 10 s for surface waves [*Visser et al.*, 2008]) was added to the synthetics. Finally, Figures 1c and 1d show the results of inverting the real *S*-wave-only and joint *S*- and surface-wave data, respectively.

[13] Comparing the top panels of Figures 1a and 1b, we notice that the input pattern is reproduced equally well in both, while amplitude is resolved much better after the introduction of surface waves (Figure 1b).

[14] In the mid-to-lower mantle, the two output models become increasingly similar with growing depth, as surface-wave sensitivity decays. At the very bottom of the mantle, the introduction of surface-wave synthetics seems to have slightly deteriorated resolution: the total number of data has grown, but the same subset sample the lowermost mantle, which has then a lower influence on the least squares fit.

[15] Different considerations are drawn from Figures 1c and 1d, i.e., from the inversion of real data. While the deep, fast roots of cratons are imaged by both *S*-wave and joint databases, expected slow regions under mid-oceanic ridges are only found when surface-wave data are inverted. This suggests that their vertical extent is too small for *S* waves alone to resolve them globally with standard methods and coverage. At large depths down to the lowermost mantle, *S*-wave and joint models converge to the same solution.

[16] Figure 2 shows how the vertical pattern of velocity heterogeneity at one location is resolved by tomography. The inferences drawn from Figure 1 are confirmed, with the joint database achieving a higher resolution than the body-wave-only one, at least in the upper to mid mantle and at this particular location. Importantly, the sharp changes in pattern that characterize the input model are smoothed significantly in the output; this effect is particularly severe at relatively shallow depth (i.e., ~500 km), and is only partially suppressed by the introduction of surface waves.

5. Spotting Minima of Vertical Coherence

[17] Figure 2 suggests that vertical changes in the heterogeneity pattern will be smeared out in tomographic inversions. We propose here the following experiment to better identify them. The Earth's mantle is parameterized

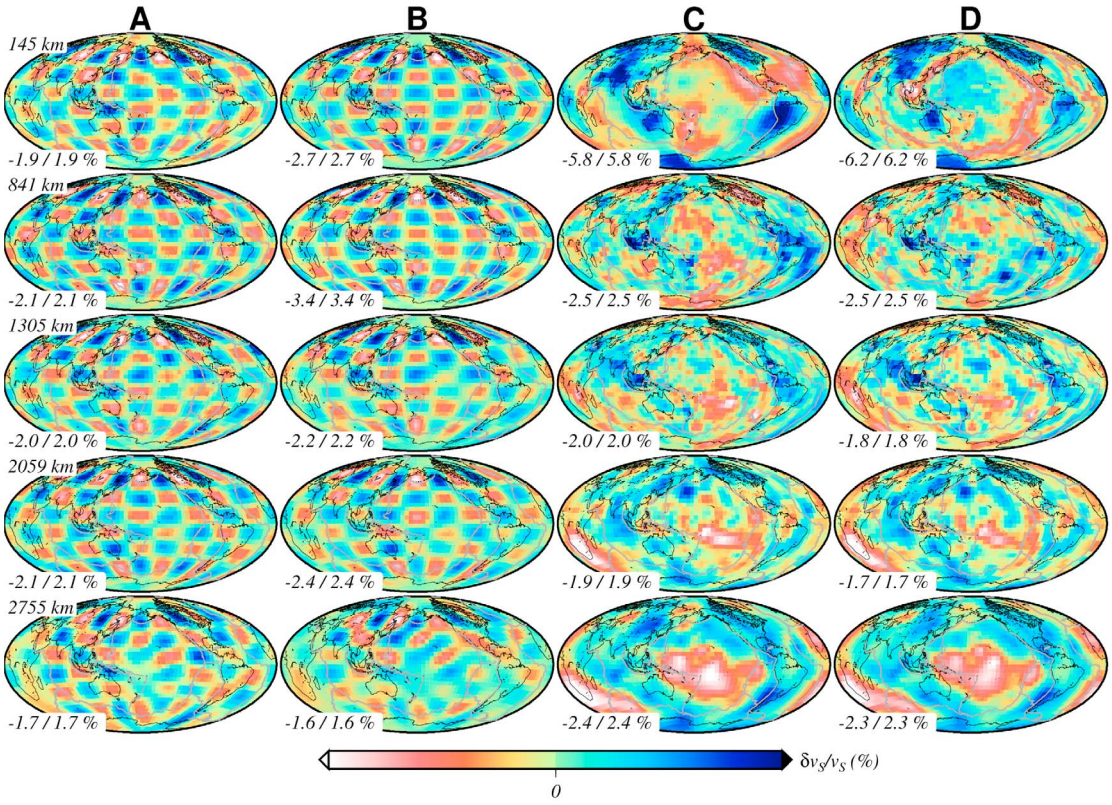

Figure 1. Four examples of tomography maps of relative *S*-velocity anomaly shown at (top to bottom) the five depths indicated on the left, and with the color code given at the bottom for minimum and maximum anomaly specified on each panel. (a) Inversion of *S*-wave only synthetic data from an input "checkerboard" model and phases and source-station geometry as by *Ritsema et al.* [2011]. (b) Inversion of *S*-wave synthetic data as in Figure 1a, combined with Love and Rayleigh-wave synthetics (source-station geometry as by *Visser et al.* [2008]). (c) Inversion of *S*-wave only observations from *Ritsema et al.* [2011]. (d) Inversion of *S*-wave data from Figure 1c, combined with Love and Rayleigh-wave data from *Visser et al.* [2008].

finely in the vertical direction, and as many tomographic inversions are conducted as there are layers in our parameterization. Inversions are regularized by minimizing both horizontal and vertical model roughness; vertical roughness minimization consists of coupling structure at one layer with that at neighboring layers only. At each inversion, the regularization scheme is changed so that the vertical roughness is not damped at one and only one layer. After iterating the procedure for all layers, we plot data variance reduction and model roughness (norm of model gradient integrated over the entire mantle) as functions of the depth of the undamped layer: depths where variance reduction is high are likely characterized by relatively important vertical changes in mantle structure, quantified by the corresponding model roughness.

[18] We first apply this algorithm to the checkerboard-based, joint body- and surface-wave synthetic data set of section 4, and show the results in Figures 3a and 3b. Here and in the following, variance reduction and roughness are normalized to those resulting from a uniform-vertical-damping, otherwise identical run. We next generate two more input models, both based on global mantle structure derived from a geodynamic forward subduction model [*Steinberger*, 2000; *Steinberger and Torsvik*, 2010] (converted from density to seismic velocity anomalies via a constant scaling factor). We here use the geodynamic model as a "typical" representation

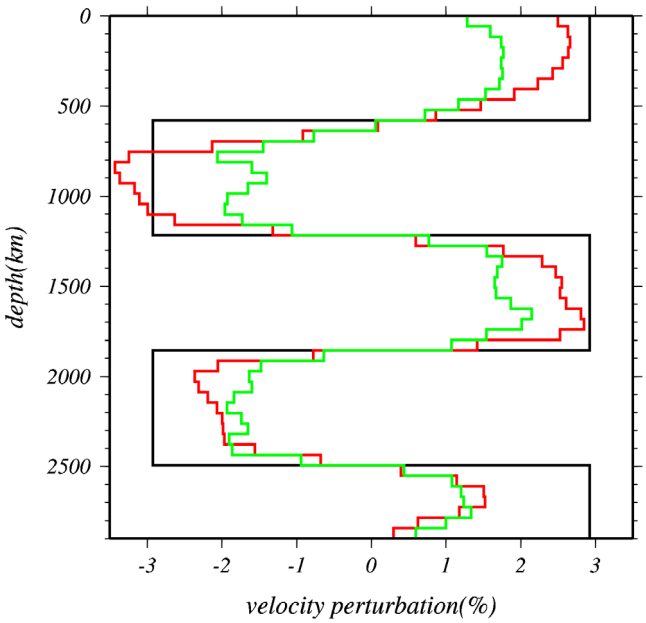

Figure 2. Input (black curve) and output synthetic models of Figure 1a (green) and Figure 1b (red) as functions of depth, at one well resolved location under the Aleutian Islands (180°W, 55°N).

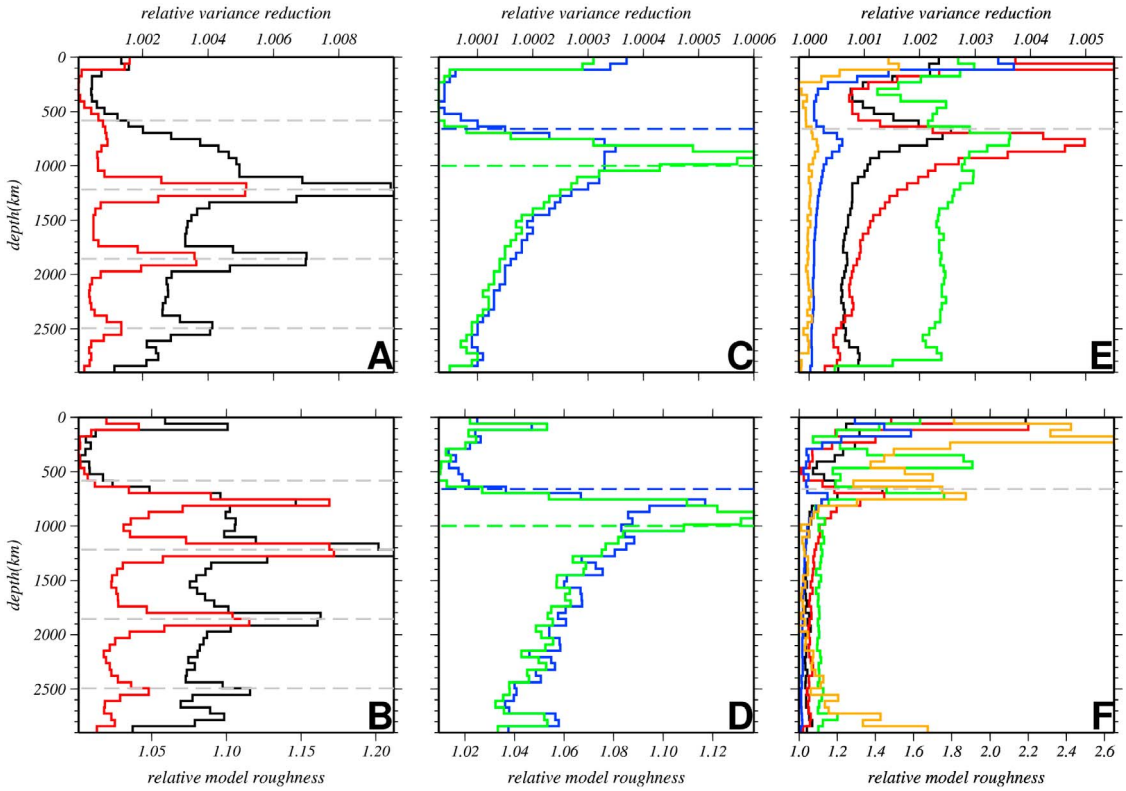

Figure 3. Applications of the algorithm of section 5. Growth in (a, c, e) variance reduction and (b, d, f) model roughness as functions of depth, for body-wave-only (black curves in Figures 3a and 3b) and combined surface- and body-wave (red, green, blue in Figures 3c and 3d) synthetics, and for real databases (Figures 3e and 3f). Results in Figures 3a and 3b are based on the checkerboard input model, with pattern changes at depths marked by gray dashed lines. The synthetics in Figures 3c and 3d, corresponding to the joint *S* and surface-wave database, are based on two "realistic" input models with vertical changes at depths of either 660 (blue) or 1000 km (green), marked by dashed lines. Different colors in Figures 3e and 3f correspond to: *P* delay times of *Antolik et al.* [2001] (black); *S* delay times of *Houser et al.* [2008] (green); *S* delay times of *Ritsema et al.* [2011], including multiply reflected phases (red); delay times of *Ritsema et al.* [2011] combined with surface-wave dispersion from *Visser et al.* [2008] (blue); delay times of *Ritsema et al.* [2011] combined with surface-wave dispersion from *Ritsema et al.* [2011] (orange). A gray dashed line in Figures 3e and 3f marks the 660.

of actual mantle structure, independent of the spatial details of the model. To simulate vertical decorrelation as could be expected from slab stagnation effects, a derived model is obtained from the original by shifting the entire lower-mantle structure by 15° eastward, over a linear transition of 150 km above the depth of 660 km; a second model is obtained by setting the top of the lower mantle at 1000 km, and repeating the same procedure. Synthetic body- and surface-wave data are then computed as in section 4, and fed to our algorithm: the results are shown in Figures 3c and 3d.

[19] Our algorithm, applied to checkerboard-based synthetics (Figures 3a and 3c), recovers successfully input vertical changes at 1200 and 1900 km depth, which appear as clear maxima in both relative increase of variance reduction (small but systematic, despite the high level of noise added to the synthetics) and model roughness. The jump at 2500 km, sampled by body-wave data only, is less prominent but still visible in the variance reduction plot (Figure 3a). Throughout the lower mantle, no spurious maxima are seen in Figure 3a away from depths of input decorrelation. The shallower input feature at 600 km is "resolved" only in the roughness plot, and smeared to a larger depth of ~800 km. The introduction of surface-wave data (compare red to black curves) improves transition-zone resolution only marginally. This confirms the limits in upper-mantle resolution by body-wave data, and the difficulty of using surface-wave observations to constrain vertical structure.

[20] Figures 3c and 3d indicate that our algorithm can resolve only partially the exact depth of pattern changes in the presence of complex 3-D structure. Both the variance-reduction (Figure 3c) and roughness (Figure 3d) plots associated with the input pattern change at 660 km place the most important vertical change at ~800 km; the input 1000-km change is more successfully mapped between ~850–1000 km.

[21] After verifying that strong vertical changes in the mantle can be at least partially resolved by our algorithm, we apply it to real data. Both relative variance reduction (Figure 3e) and model roughness (Figure 3f), independent of the inverted database (*P*, *S*, and joint *S* and surface waves), are characterized by two prominent maxima roughly at the base of the lithosphere (~100 km depth) and upper-to-lower mantle discontinuity (~800 km depth). From the comparison of Figures 3e and 3f with Figures 3a–3d we infer that part of the lithosphere signature could be an artifact of limited resolution; the ~800-km pattern change, on the other hand, is robust and largely independent of inverted subset of data, and likely reflects a global signature of slab ponding [e.g.,

Fukao et al., 2001; *Gu et al.*, 2003; *Obayashi et al.*, 2009], perhaps at depths larger than the 660 discontinuity itself. Below 660 km, relative variance reduction decays with depth, while relative model roughness is uniformly low. The only exception is a kink in both metrics at ~2600 km, presumably associated with the top of the D″.

[22] In general, the lower mantle appears to be much more vertically coherent than the upper mantle, independently of the inverted data. Yet, strong vertical gradients at depths between ~1000 and ~2000 km would be resolved well by our method. We infer that the pattern of lower-mantle heterogeneity changes very smoothly in the vertical direction. This is contrary to earlier suggestions of vertical decorrelation and inconsistent with global layering, provided that laterally varying topography associated with the latter be relatively small [e.g., *Kellogg et al.*, 1999].

6. Conclusions

[23] We have developed and validated a tomography-based method to identify depth ranges of globally strong vertical gradients in seismically mapped structure in the Earth's mantle. We have applied it to a number of different seismic databases, including *P* and *S* travel times and the dispersion of surface-wave overtones and fundamental modes. We find that, while helping to constrain the horizontal pattern of velocity heterogeneity in the upper mantle, surface-wave data improve only marginally our resolution of the vertical dependence of heterogeneity in the transition zone: this is a consequence of surface-wave modes being sensitive to velocity structure over very wide depth ranges [e.g., *Visser et al.*, 2008]. Our results suggest that the transition between Earth's upper and lower mantle is indeed characterized by important vertical heterogeneity, maximum at a depth close to 660 km, but that could be as large as ~800 km. The lower mantle is predominantly vertically coherent.

[24] **Acknowledgments.** This manuscript benefitted from the comments of Michael Wysession and two anonymous reviewers. We are very grateful to all the seismologists who shared their databases, and to B. Steinberger for sharing his subduction model. Y. Gu helped greatly with the implementation of radially anisotropic *S* travel-time kernels. J. Yu assisted us in porting our software to the USC Earth Sciences computer cluster. All figures were generated with the Generic Mapping Tools software [*Wessel and Smith*, 1991]. LB thanks D. Giardini for his support and encouragement. This research was partially supported by NSF-EAR 0910985.

[25] The Editor wishes to thank Christine Houser and an anonymous reviewer for their assistance evaluating this paper.

References

Antolik, M., G. Ekström, and A. M. Dziewonski (2001), Global event location with full and sparse data sets using three-dimensional models of mantle P-wave velocity, *Pure Appl. Geophys.*, *158*, 291–317.

Becker, T., and L. Boschi (2002), A comparison of tomographic and geodynamic mantle models, *Geochem. Geophys. Geosyst.*, *3*(1), 1003, doi:10.1029/2001GC000168.

Boschi, L., and A. M. Dziewonski (1999), High- and low-resolution images of the Earth's mantle: Implications of different approaches to tomographic modeling, *J. Geophys. Res.*, *104*, 25,567–25,594.

Boschi, L., and G. Ekström (2002), New images of the Earth's upper mantle from measurements of surface wave phase velocity anomalies, *J. Geophys. Res.*, *107*(B4), 2059, doi:10.1029/2000JB000059.

Boschi, L., T. W. Becker, and B. Steinberger (2007), Mantle plumes: Dynamic models and seismic images, *Geochem. Geophys. Geosyst.*, *8*, Q10006, doi:10.1029/2007GC001733.

Bower, D. J., M. Gurnis, J. M. Jackson, and W. Sturhahn (2009), Enhanced convection and fast plumes in the lower mantle induced by the spin transition in ferropericlase, *Geophys. Res. Lett.*, *36*, L10306, doi:10.1029/2009GL037706.

Courtillot, V., A. Davaille, J. Besse, and J. Stock (2003), Three distinct types of hotspots in the Earth's mantle, *Earth Planet. Sci. Lett.*, *205*, 295–308.

Della Mora, S., L. Boschi, P. J. Tackley, T. Nakagawa, and D. Giardini (2011), Low seismic resolution cannot explain S/P decorrelation in the lower mantle, *Geophys. Res. Lett.*, *38*, L12303, doi:10.1029/2011GL047559.

Dziewonski, A. M., and D. L. Anderson (1981), Preliminary reference Earth model, *Phys. Earth Planet. Inter.*, *25*, 297–356.

Dziewonski, A. M., V. Lekic, and B. A. Romanowicz (2010), Mantle Anchor Structure: An argument for bottom up tectonics, *Earth Planet. Sci. Lett.*, *299*, 69–79, doi:10.1016/j.epsl.2010.08.013.

Fukao, Y., S. Widiyantoro, and M. Obayashi (2001), Stagnant slabs in the upper and lower mantle transition region, *Rev. Geophys.*, *39*, 291–323.

Grand, S. P., R. D. van der Hilst, and S. Widiyantoro (1997), Global seismic tomography: A snapshot of convection in the Earth, *GSA Today*, *7*, 1–7.

Gu, Y. J., A. M. Dziewonski, and G. Ekström (2003), Simultaneous inversion for mantle shear velocity and topography of transition zone discontinuities, *Geophys. J. Int.*, *154*, 559–583.

Houser, C., G. Masters, P. Shearer, and G. Laske (2008), Shear and compressional velocity models of the mantle from Cluster analysis of long-period waveforms, *Geophys. J. Int.*, *174*, 195–212.

Kellogg, L. H., B. H. Hager, and R. D. van der Hilst (1999), Compositional stratification in the deep mantle, *Science*, *283*, 1881–1884.

Mooney, W. D., G. Laske, and T. G. Masters (1998), CRUST 5.1: A global crustal model at 5° × 5°, *J. Geophys. Res.*, *103*, 727–747.

Nataf, H.-C., I. Nakanishi, and D. L. Anderson (1984), Anisotropy and shear-velocity heterogeneities in the upper mantle, *Geophys. Res. Lett.*, *11*, 109–112.

Obayashi, M., J. Yoshimitsu, and Y. Fukao (2009), Tearing of stagnant slab, *Science*, *324*, 1173–1175.

Panning, M. P., V. Lekić, and B. A. Romanowicz (2010), Importance of crustal corrections in the development of a new global model of radial anisotropy, *J. Geophys. Res.*, *115*, B12325, doi:10.1029/2010JB007520.

Puster, P., and T. H. Jordan (1997), How stratified is mantle convection?, *J. Geophys. Res.*, *102*, 7625–7646.

Ritsema, J., A. Deuss, H. J. van Heijst, and J. H. Woodhouse (2011), S40RTS: A degree-40 shear-velocity model for the mantle from new Rayleigh wave dispersion, teleseismic traveltime and normal-mode splitting function measurements, *Geophys. J. Int.*, *184*, 1223–1236.

Steinberger, B. (2000), Slabs in the lower mantle—Results of dynamic modelling compared with tomographic images and the geoid, *Phys. Earth Planet. Inter.*, *118*, 241–257.

Steinberger, B., and T. H. Torsvik (2010), Toward an explanation for the present and past locations of the poles, *Geochem. Geophys. Geosyst.*, *11*, Q06W06, doi:10.1029/2009GC002889.

Tackley, P. J. (2000), Mantle convection and plate tectonics: Toward an integrated physical and chemical theory, *Science*, *288*, 2002–2007.

Tackley, P. J. (2002), Strong heterogeneity caused by deep mantle layering, *Geochem. Geophys. Geosyst.*, *3*(4), 1024, doi:10.1029/2001GC000167.

van der Hilst, R. D., and T. Seno (1993), Effects of relative plate motion on the deep structure and penetration depth of slabs below the Izu-Bonin and Mariana island arcs, *Earth Planet. Sci. Lett.*, *120*, 395–407.

Visser, K., J. Trampert, and B. L. N. Kennett (2008), Global anisotropic phase velocity maps for higher mode Love and Rayleigh waves, *Geophys. J. Int.*, *172*, 1016–1032.

Wessel, P., and W. H. F. Smith (1991), Free software helps map and display data, *Eos Trans. AGU*, *72*(41), 441.

Woodhouse, J. H. (1981), A note on the calculation of travel-times in a transversely isotropic Earth model, *Phys. Earth Planet. Inter.*, *25*, 357–359.

T. W. Becker, Department of Earth Sciences, University of Southern California, MC 0740, Los Angeles, CA 90089-0740, USA.

L. Boschi, Institute of Geophysics, ETH Zurich, Sonnesggstrasse 5, CH-8092 Zurich, Switzerland.